JOURNAL OF MATERIALS SCIENCE 5 (1970) 63–81

A Terminal Ballistics Application of Transmission Electron Microscopy: The Anatomy of a Bullet Hole

L. E. MURR, J. V. FOLTZ*
Departments of Materials Science and Electrical Engineering,
University of Southern California, Los Angeles, California, USA

A novel technique was devised for the selected area observation of residual microstructures in the deformation zones and the detached cap sections of .22 calibre bullet holes in thin sheets and laminate thicknesses ranging from 0.03 to 0.54 mm of 304 stainless steel and Inconel 600 by bright- and dark-field transmission electron microscopy. Microhardness measurements over the detached cap and petals, extending radially into the undeformed material, indicated the zone of action to be confined to a region bounded by the deviation of the impact zone from the plane of the plate. This feature was confirmed by electron microscope observations which indicated no defects beyond the bounds of the zone of action so defined. Residual microhardness was observed to increase from the radial bound of the zone of action toward the axis of projectile motion, with maximum hardness values roughly twice the undeformed sheet hardness observed in the petal edges and the detached caps. Dislocation densities were observed to increase correspondingly over this range ($\sim 10^6$ to 10^{11} cm^{-2}), with deformation twins occurring in the petal edges and the detached caps of both materials. An analytical treatment of the specific ballistic perforation examined in this investigation based on the plastic stretching of the target zone of action, fracture and detachment of a cap, and the subsequent petalling of the crater as perforation commences, indicated an absence of high pressure shock effects.

1. Introduction

As a general branch of applied physics, ballistics can be divided into three categories: interior ballistics, the study of projectile motion while constrained by a gun tube; exterior ballistics, the study of a projectile in flight, and terminal ballistics, the study of the interaction of a projectile with a target. Our understanding of terminal ballistic phenomena is in general not commensurate with that of interior or exterior ballistics, primarily because the extremely small time intervals associated with impact phenomena make detailed experimentation during target attack difficult. The specific problem of armour penetration and perforation is further complicated by its military nature, which renders much of the relevant literature inaccessible due to classification.

The thin-skin construction of modern aircraft and the armouring of space vehicles against meteor attack makes an understanding of thin plate perforation essential. Our ability to tailor-make materials having a resistance to high-velocity impact damage while maintaining specific structural-mechanical functions over a range of environmental conditions also demands a fundamental knowledge of the physical behaviour of the material. The ability to define the work-hardening in industrially punched parts, and to elucidate clearly the residual plastically deformed zones in a manufactured hardware item produced by a forging technique could, in

---

*Permanent address: Materials Science Division, US Naval Weapons Laboratory, Dahlgren, Virginia, USA.

addition to advancing technology, aid in clarifying the basic tenets of plasticity theory.

Several analytical and physical models have been proposed to explain the processes associated with the impact, penetration and perforation of ductile metal plates which deform plastically [1-6], and penetration and perforation have been investigated experimentally [7-9]. Theoretical treatments of the problem require the making of many idealised approximations [10-12], and the experimental considerations of elastic-plastic plate penetration have involved specific characteristics of the striking projectile shape, velocity, and composition, and specific armour materials [13, 14] without regard for the materials properties.

Realising that the complete characterisation of the processes which occur during impact, penetration, and perforation cannot be accomplished in a single investigation, the present study proposes, through a rather novel application of transmission electron microscopy, the direct observation of the residual deformation in the immediate area of perforation in a thin plate. It is implied in this approach that if the mode of failure in thin armour plate can be determined by direct observation of residual defect structures, then the metallurgical properties governing the ballistic behaviour of the material can be better understood. The ultimate aim would then involve incorporating the basic principles of defect physics with the engineering of materials intended to resist ballistic attack.

In view of the sociological trends in the United States and the world in general, the mode of armour penetration and the choice of emphasis in this investigation (as expressed specifically in the title of this paper) is, for the most part, pragmatic, and specific military implications are unintentional. It is the purpose of this investigation to illustrate the powerful direct approach to the study of perforation and punching mechanics afforded by the use of conventional electron microscopes.

2. Analytical Considerations

The collision of a projectile with a flat metal plate is a very complex phenomenon, involving in the general case such factors as work-hardening effects, heat-conduction, crack-formation, elastic and plastic wave-propagation, and strain-rate effects. The present experiments were limited to metal target plates that were "thin", i.e. the ratio of the diameter of the projectile to the thickness of the plate was at least 10. For the present considerations, the mode of plate deformation will be described as a "cap and petalling" process. In this process the penetration phenomena are assumed to occur in three stages: the formation of a cap of the metallic plate on the projectile head; the separation of the cap from the plate proper; and the petalling of the foil in the area adjacent to the hole left by removal of the cap as shown in fig. 1. Energy is lost by the bullet to each stage of the penetration process, at first to plastic deformation and fracture of the metallic cap and then, as the petals are created, because of friction between the bullet and the inner wall of the crater.

For reasons of comparison with other types of deformation of the same materials, it is desirable to estimate the magnitude of stress induced in the cap by the striking projectile. Following former theoretical approaches to problems of this type [3, 10, 11], we will consider an idealised model of the collision of a projectile with a plate at normal incidence. For the velocity and plate thickness of the present experimental material, strength effects are expected to be a minor factor, so it will be assumed that the energy lost by the projectile to plastic deformation of the cap may be obtained by utilising the displacement configuration under static conditions. Such a procedure was followed by Thomson [11] in making a similar ballistic analysis. The instantaneous velocity of the projectile as the cap is being formed can be determined from momentum considerations. Choosing an axis of reference along the direction of motion, the law of momentum conservation yields

$$(m + M(r_0))\,\mathrm{d}v + v\mathrm{d}M(r_0) = -\frac{\mathrm{d}W_\mathrm{p}}{v}, \quad (1)$$

In equation 1, m is the mass of the projectile, $M(r_0)$ is the instantaneous mass of the cap, v is the instantaneous velocity of the projectile-cap unit, and $\mathrm{d}W_\mathrm{p}$ is the energy required to deform the element of mass $\mathrm{d}M(r_0)$, plastically. For a precise solution of the problem within the limits of the present model, equation 1 should be integrated to yield the velocity of the projectile at the instant of fracture. However, when the total mass of the cap at the instant of fracture is only a small fraction of the projectile mass, a reasonably accurate solution to equation 1 can be obtained by setting the initial momentum of

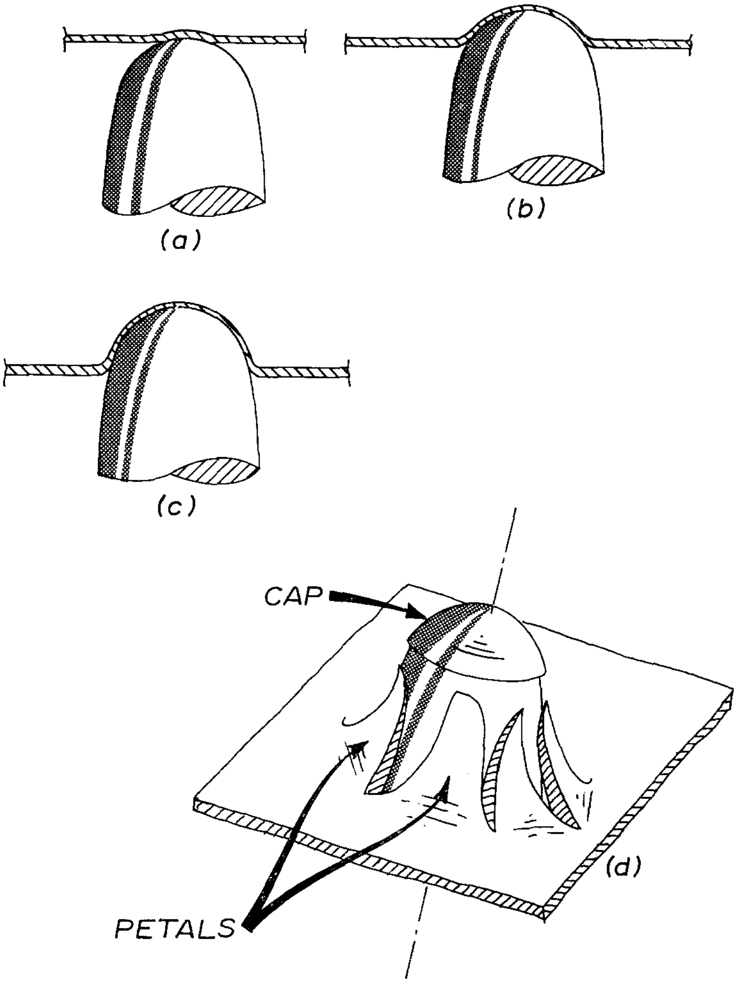

Figure 1 Progressive stages in ballistic penetration and perforation of a thin target material. (a) Early state of penetration; (b) high-velocity straining of the target in the zone of action; (c) onset of fracture; (d) 3-dimensional view of the detachment of the strained cap and the formation of petals in the crater as perforation reaches completion.

the system equal to the momentum of the system at the instant of fracture:

$$(m + M_c)\, v_f = m v_s - \frac{\Delta W_p}{v_s}\,, \qquad (2)$$

where M_c is the mass of the entire cap, v_f is the velocity of the projectile-cap unit when fracture occurs, and v_s is the striking velocity of the projectile.

Consider next the work required to deform the cap plastically. In the initial stage of the impact, the flat target plate is bent to fit the curved shape of the projectile head. An element of foil which originally occupied the area $\mathrm{d}A = r_0 \mathrm{d}r_0 \mathrm{d}\theta$, where θ is the polar angle will, after the collision, occupy the area $\mathrm{d}A' = r_0 \mathrm{d}s \mathrm{d}\theta$ as shown in fig. 2. The amount the foil is stretched is

$$\mathrm{d}S = \mathrm{d}s - \mathrm{d}r_0, \qquad (3)$$

where ds is an element of length measured tangential to the projectile head, and

$$\mathrm{d}s = \sqrt{((\mathrm{d}r_0)^2 + (\mathrm{d}z)^2)}. \qquad (4)$$

The work done in stretching the element of foil is

$$\sigma_Y t_0 r_0 \mathrm{d}\theta \, \mathrm{d}S, \qquad (5)$$

where σ_Y is the material yield stress and t_0 is the foil thickness. The work required to deform the entire ring of radius r_0 is

$$\mathrm{d}W_{r0} = \sigma_Y t_0 2\pi r_0 \mathrm{d}S. \qquad (6)$$

If the work done on all such rings from $r_0 = 0$ to $r_0 = r_f$ is summed, the total energy required for the plastic deformation becomes

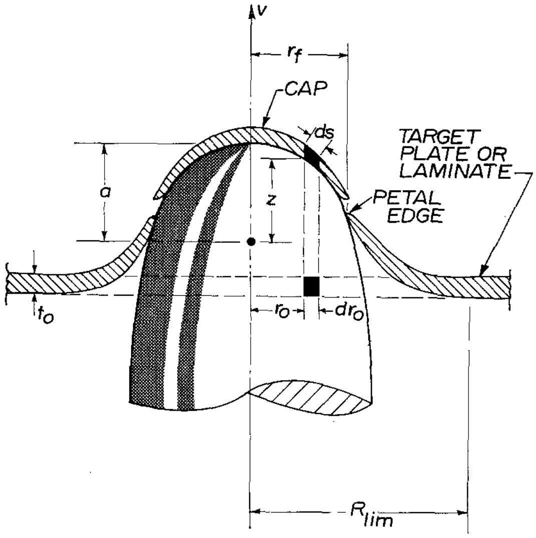

Figure 2 Section view of perforation geometry at stage (d) of fig. 1.

$$\Delta W_p = \int_0^{r_f} \sigma_Y t_0 2\pi r_0 \left[\sqrt{1 + \left(\frac{dz}{dr_0}\right)^2} - 1\right] dr_0. \tag{7}$$

Such an equation is perfectly general and can be applied to any known shape of projectile and any radius of fracture r_f. In the present case the tip of the projectile head can be approximated by a hemispherical surface. The tip is then described by the equation

$$a = \sqrt{(r_0^2 + z^2)}, \tag{8}$$

where a is the radius of the hemisphere.

Thus

$$\frac{dz}{dr_0} = -\frac{r_0}{\sqrt{a^2 - r_0^2}}, \tag{9}$$

and

$$\Delta W_p = \int_0^{r_f} \sigma_Y t_0 2\pi r_0 \left[\frac{a}{\sqrt{a^2 - r_0^2}} - 1\right] dr_0. \tag{10}$$

If the yield stress is not a function of the total plastic work done, then

$$\Delta W_p = \sigma_Y t_0 2\pi \left[a^2 - a\sqrt{a^2 - r_f^2} - \frac{r_f^2}{2}\right]. \tag{11}$$

With the aid of equation 11, we can now solve equation 2 for the projectile velocity at the instant of fracture, v_f. The average impulse along the direction of motion delivered to the projectile head by the cap is then

$$\bar{F}\Delta t = m(v_s - v_f), \tag{12}$$

where Δt is the time in which the collision took place. The collision time is obtained by setting $r_0 = r_f$ in equation 8 and obtaining $z(r_f)$, from which

$$\Delta t = \left[\frac{a - z(r_f)}{v_s}\right]. \tag{13}$$

The average stress along the direction of motion is then

$$\bar{\sigma} = \frac{\bar{F}}{\pi r_f^2}. \tag{14}$$

We can also consider the residual petal mass following perforation to be given approximately by

$$M = \frac{m_T - M_c}{n}, \tag{15}$$

where m_T is the total mass of plate material within the zone of action, and n is the number of petals. If R_{lim} is the radius of the zone of action on the original plate (fig. 2), then

$$n = \left(\frac{\pi R^2_{lim}\,\rho}{M}\right) t_0 - \frac{M_c}{M}. \tag{16}$$

3. Experimental Methods

On considering the ultimate goal of this investigation, namely the characterisation of the damage inflicted in a metallic material by projectile penetration and perforation, it was decided at the outset to use materials which bore some relationship to general armouring applications, e.g. the carburised steels (cemented armours) used in heavy military applications (having a composition of 0.4 to 0.5% C, 3.5 to 4% Ni, 1 to 3% Cr, 0.4 to 1% Mn, 0.1 to 0.2% Si, balance Fe) [15], heat-treated Ni–Cr alloys for light armour and deck armour, Hadfield steel body armour [15]; and the variety of special alloy superstructures of aircraft and related air and spacecraft. In addition, it seemed desirable to investigate materials which were industrially significant and bearing some relationship to industrial high-speed punching and similar applications, structurally simple materials, materials easily thinned for direct observation by transmission electron microscopy; and preferably materials already extensively studied with respect to related modes of plastic deformation, e.g. explosive shock-loading. The final choice consisted of two materials: type 304 stainless steel and Inconel 600 alloy.

3.1. Experimental Arrangement

Stainless steel and Inconel test materials having nominal compositions indicated in table I were initially in sheet form having thicknesses of 0.18 and 0.025 mm respectively. Each alloy was subject to a rapid sheet anneal for 0.25 h at 1060° C. This treatment produced a residual grain size of 15 to 20 μm in both materials, and in addition produced a fairly homogeneous distribution of fine, coherent precipitates (carbide) in the Inconel.

The stainless steel and Inconel sheet materials were cut into 2.5 cm squares and mounted in single and laminated sections on a thick wood foundation. Two samples of stainless steel were mounted as single sheets, and three each for laminates of two and three sheets. The sample thicknesses to be penetrated then consisted of 0.18, 0.36 and 0.54 mm respectively. Two Inconel samples were mounted as single sheets, while three samples each of laminated thicknesses of 0.09, 0.18 and 0.36 mm were also mounted on the same foundation. This arrangement allowed the projectiles to be recovered without difficulty.

The thin sheet samples were perforated with .22 calibre bullets (high-speed long rifle) fired at normal incidence from a distance of 10 ft. The projectiles were characterised by a hemispheric head, weighed 2.59 g; and had a nominal striking velocity of 405 msec^{-1}. In all cases, the bullets perforating the metallic samples penetrated into the wood foundation a depth of approximately 5.7 cm, and were manually removed so that the extracted hole section or cap attached to the face of the projectile could be recovered for examination.

3.2. Microhardness Measurements

It was initially desirable to have some indication of the deformation at the point of perforation as well as an evaluation of the radial extent of damage from the actual bullet hole. Because of the ability of Vickers microhardness indentations to give relative measures of defect densities as demonstrated repeatedly in numerous investigations involving explosive shock-loading and related modes of deformation [16-20], it seemed obvious that this approach could produce reliable indications of the work-hardening trends of interest in the present investigation.

In one series of measurements, the stainless steel caps were lightly electropolished in an electrolyte consisting of 42% H_3PO_4, 34% H_2SO_4 and 24% H_2O. Microhardness measurements were then made on the exit surface (convex) of the stainless steel caps using a 100 g load. The indentations were confined to an area of roughly 0.3 mm^2 at the centre, and consisted of a maximum of 10 indentations spaced approximately 0.2 mm apart over this area. Similar measurements were made on the Inconel cap extracts using a 50 g load. The single sheet Inconel cap extracts were not recovered, and those measurements for the remaining Inconel perforation experiments were made on the exit surface with no prior polishing.

Fig. 3 illustrates the manner in which the hardness profile from the bullet hole was measured in the perforated sheets. The technique consisted in first cutting the sheet section in half. The petals were then flattened between polished stainless steel blocks (by pressing together by hand so as not to induce excessive deformation). When pressed flat, the diameter of the hole was measured and compared with the diameter of the cap recovered from the projectile surface as a measure of the total strain. The stainless steel sheets were lightly electropolished while the Inconel sheets were left unpolished (these were already in polished form in the annealed sheet). Radial strips were then cut from the penetration zone (as shown in fig. 3) which measured approximately 2 mm in width, and which normally followed a petal.

With the petal edge (hole edge) positioned at the cross-hairs in the microhardness tester, the test strip (after final flattening) was translated 0.50 mm using the calibrated stage and five equally spaced indentations were made along the width of the strip beginning approximately 0.5 mm from the edge using 100 and 50 g loads for the stainless steel and Inconel strips respectively. The strip was then translated continuously in increments of 0.5 mm from the petal edge and the process repeated. Normally two test strips were taken from each sheet of a laminated

TABLE I Specimen composition (wt %)

Material	Fe	Ni	Cr	Cu	Mn	Si	C	Co
304 stainless steel	70.39	9.52	18.43	0.14	1.05	0.42	0.06	—
Inconel 600	7.30	76.26	15.91	0.02	0.13	0.28	0.06	0.01

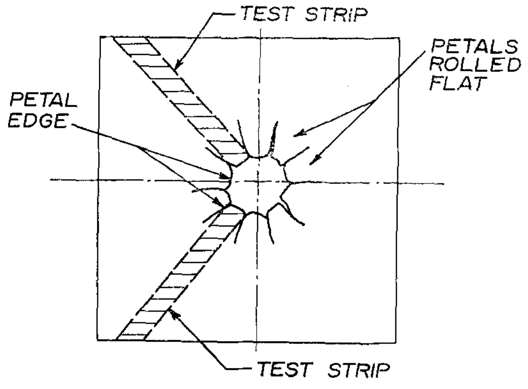

Figure 3 Schematic illustration of the method of extracting test strips from a perforated plate for microhardness measurements.

sample and microhardness measurements made on both entrance and exit surfaces. The microhardness values for corresponding displacements from the petal edge were then averaged where appropriate.

3.3. Selected-Area Examination by Transmission Electron Microscopy

A technique previously described by Murr [21] was utilised in a slightly modified form to produce electropolished thin sections at regular radial intervals from the edge of a perforation in the electrolyte previously described, and employing a constant potential level of 9.5 V for pointed stainless steel cathodes positioned 0.5 to 1 mm from the sample surfaces. The procedure involved first cutting the perforated sheet along a diameter through the hole as shown in fig. 3, then positioning the cathode centre line at some point from the edge between which the thin section was to be produced. As a general rule, sections 1 mm in width could be selectively thinned because this was the normal control over the approach of two electropolished edges. Thus, for example, by first polishing a hole about 6 mm from the edge of a perforation in the centre of a petal, another hole could then be electropolished about 2 mm closer to the perforation edge, and the electropolished holes allowed to converge. This process was repeated several times on a single petal or on adjoining petals around a perforation, and the distance from the thin node to the edge measured directly. Fig. 4 illustrates the various steps in the production of selected thin areas. It should be noted that in thinning the area at the edge of the perforation, the cathodes were positioned along the petal edges about 1 mm from the perforation edge. Electron transparent nodes were then formed within 0.5 mm from the perforation edge as shown in figs. 4e and f.

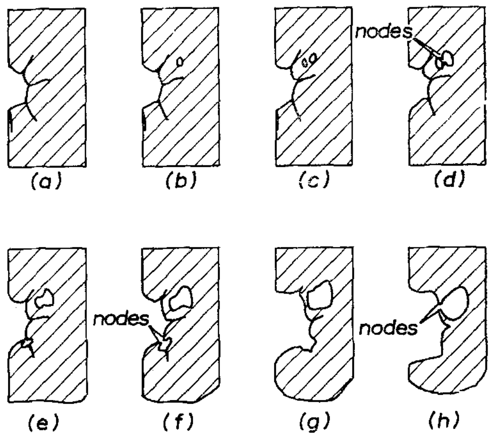

Figure 4 Schematic illustration of the preparation of selected-area foil specimens from the zone of action of a bullet hole by electrolytic polishing. (a) Half portion of perforated plate as shown in fig. 3 is mounted in electropolisher. (b) Hole is electropolished in a petal region as shown. (c) Second hole is electropolished close to first. (d) Holes are allowed to converge forming electron transparent nodes which are cut from the section. (e) Third hole is polished between petals and allowed to form nodes as shown in (f). The original two holes are utilised in forming a new set of nodes, (g) and (h). Each set of nodes in (d), (f), and (h) are located at different radial distances from the original petal edges which are directly measured with a polar scale.

By placing the electropolished sample on a polar scale, the distance of the electron-transparent node from the edge of the bullet hole was measured directly. The node was then cut from the sample. These specimens were then positioned in the electron microscope specimen holder with the thin node symmetrically aligned. The specimens were observed in a Hitachi HU 125 electron microscope operated at 125 kV, employing a goniometer tilt stage, and utilising both bright- and dark-field transmission techniques.

4. Results

The measurements of residual hardness including that of the exit side of the hole-extract and the averages of both sides of test strips (fig. 3) for various laminated and single plate thicknesses in the petal regions of the perforation are portrayed in figs. 5 and 6. The general character of the curves for stainless steel and Inconel are observed to differ quite markedly, with little apparent variation in the zone of action (R_{lim} of fig. 2) for variations of the total thickness of Inconel sheet perforated. Considerable variation is, however, apparent as the thickness of the stainless steel is changed (fig. 5). It is also observed that a marked increase in hardness in the Inconel cap occurs for all thicknesses perforated, but that the stainless steel cap hardness is practically the same as that of the petal edges. This feature might be due to temperature differences in these regions, but as we will discuss later, this phenomenon probably has no simple explanation.

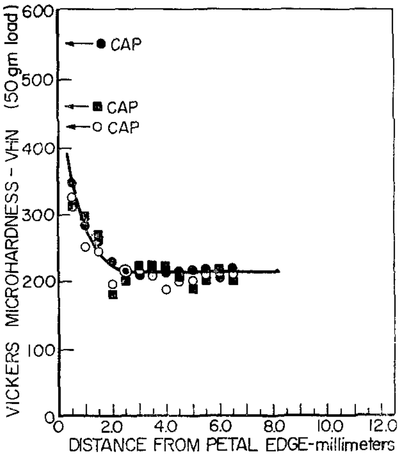

Figure 6 Average hardness profiles for perforations in laminated plates of Inconel 600 alloy. ●, Inconel 0.09 mm (0.003 in.); ○, Inconel 0.18 mm (0.007 in.); ■, Inconel 0.36 mm (0.014 in.).

Fig. 7 shows actual photographs of central cross-sectional views of several perforated plates cut through a petal. Fig. 7a is the bottom plate of a perforated 3-plate laminate of stainless steel while Fig. 7b shows the corresponding section view of perforation of a single stainless steel plate corresponding to the characteristic sections of fig. 5. Fig. 7c shows, for comparison, the bottom plate of a perforated 3-plate laminate of

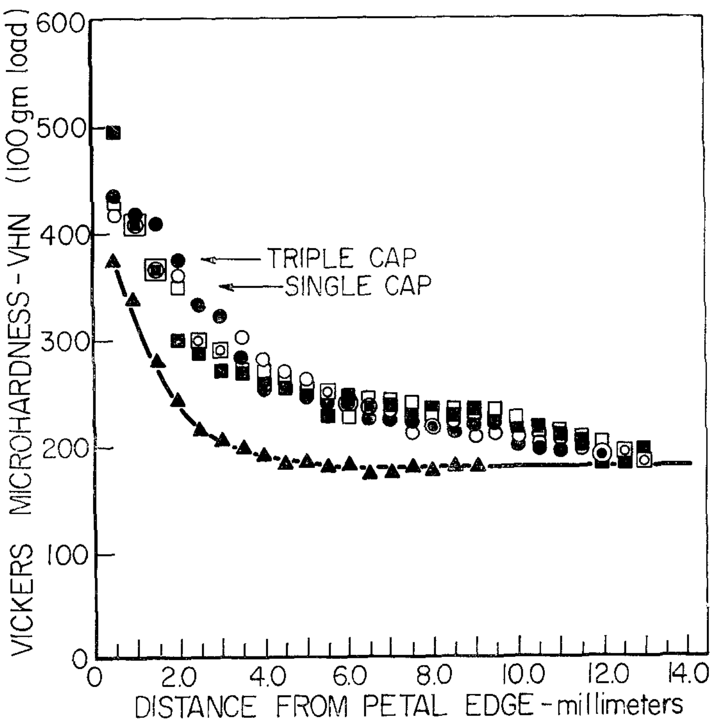

Figure 5 Average hardness profiles for perforations in laminated and single plates of 304 stainless steel. ○ Top plate + ● middle plate + □ bottom (entrance surface) + ■ bottom (exit serface) = triple laminate 0.54 mm (0.021 in.) thick. ▲ = single plate 0.18 mm (0.007 in.) thick.

Inconel. The different deformation characteristics (and response to perforation) evident on comparing figs. 5 and 6 are clearly illustrated in fig. 7, from which the corresponding zones of action as defined in fig. 5 can be measured directly.

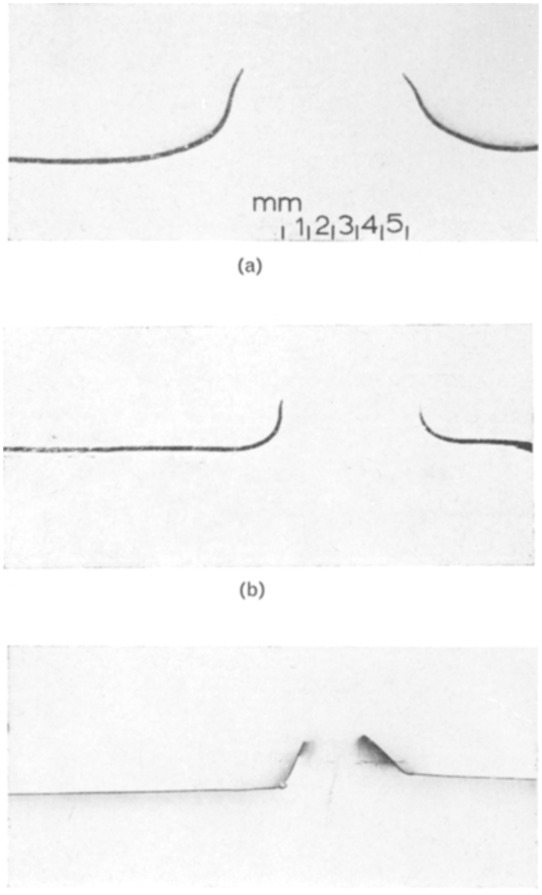

(a)

(b)

(c)

Figure 7 Photographic section views of bullet holes in single and laminated sheet thicknesses. (a) Bottom (exit) plate of a 3-plate laminate of 304 stainless steel; (b) single plate perforation in 304 stainless steel; (c) bottom (exit) plate of a 3-plate laminate of Inconel 600 alloy.

It was observed that characteristic petalling in the perforated stainless steel plates was not as well defined as in the Inconel. Considerably more dishing occurred in the stainless steel; and this obviously reflects a greater ductility in the stainless steel. These different materials characteristics are evident in the residual hardness responses shown in figs. 5 and 6, and readily apparent in the photographs of fig. 7.

The resulting observations of the deformation zones in the petal regions by transmission electron microscopy were primarily identical in each material for a corresponding average hardness as shown in figs. 5 and 6. Some differences were observed on comparing first and last plates of a laminated thickness perforation, but the effects were, for the most part, due to the contact characteristics of the plate and projectile; and the depositing of lead from the projectile on the entrance surface penetration zone which sometimes complicated the preferential thinning of regions of interest.

We will illustrate the representative microstructural features of the deformation zones associated with thin plate ballistic perforation by examining the residual petal deformation structures in the bottom (exit) plate of a 3-plate laminate thickness of both stainless steel and Inconel, corresponding essentially to the sections photographed in figs. 7a and c respectively. The corresponding microhardness measurements for individual indentations on the exit surface of the bottom plate petal test strip (fig. 3) are shown in figs. 8 and 9 for stainless steel and Inconel respectively. The curves of figs. 8 and 9 are observed to overlap, essentially, those corresponding curves of figs. 5 and 6.

Figs. 10 and 11 show the typical residual deformation microstructures for stainless steel and Inconel in the corresponding petal regions indicated in figs. 8 and 9. The microstructures in the petals not within the zone of action (R_{lim} of fig. 2) corresponding to the undeformed microhardness as shown in figs. 8 and 9, are characteristic of the undeformed material. Just within the zone of action as shown in figs. 10 and 11, regions 4 and 3 respectively, the deformation is characteristic of stage I work-hardening with numerous dislocation pile-ups and generally planar arrays of dislocations observed. Regions 3 and 2 in fig. 10 and region 2 in fig. 11 are all essentially characteristic of stage II work-hardening, with region 2 of fig. 10 for stainless steel probably representative of the end of stage II. Region 1 in both figs. 10 and 11 is characteristic of stage III work-hardening with deformation twinning constituting a significant portion of the deformation microstructure. The fact that twinning occurs profusely in the petal edges suggests that considerable shearing takes place in this region, perhaps as a result of the fracture and

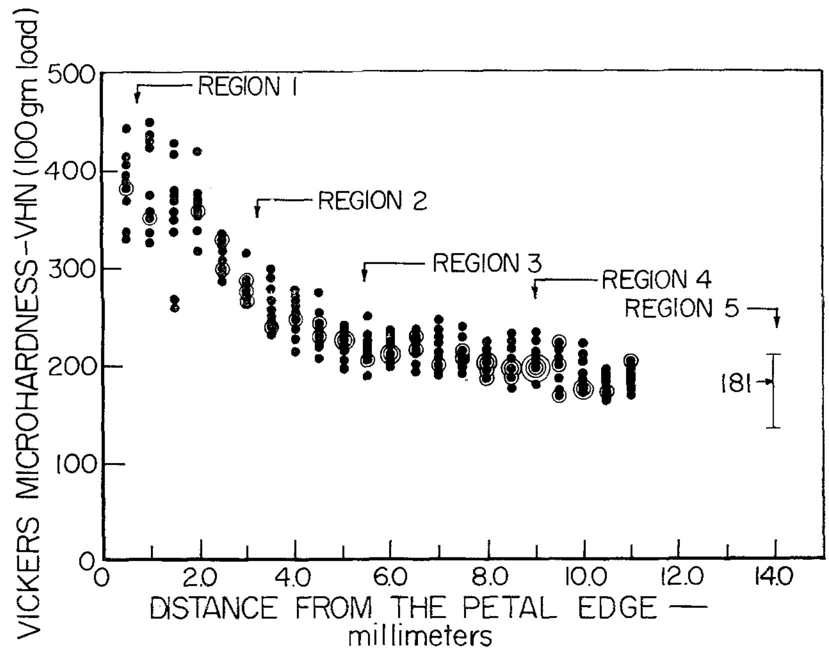

Figure 8 Typical hardness profile data for a petal test strip from the bottom (exit) plate of a 3-plate laminate of 304 stainless steel. Points plotted represent hardness values corresponding to the exit surface of the test strip. The undeformed sheet hardness is indicated as region 5. The designated regions refer to the approximate locations of areas observed by transmission electron microscopy.

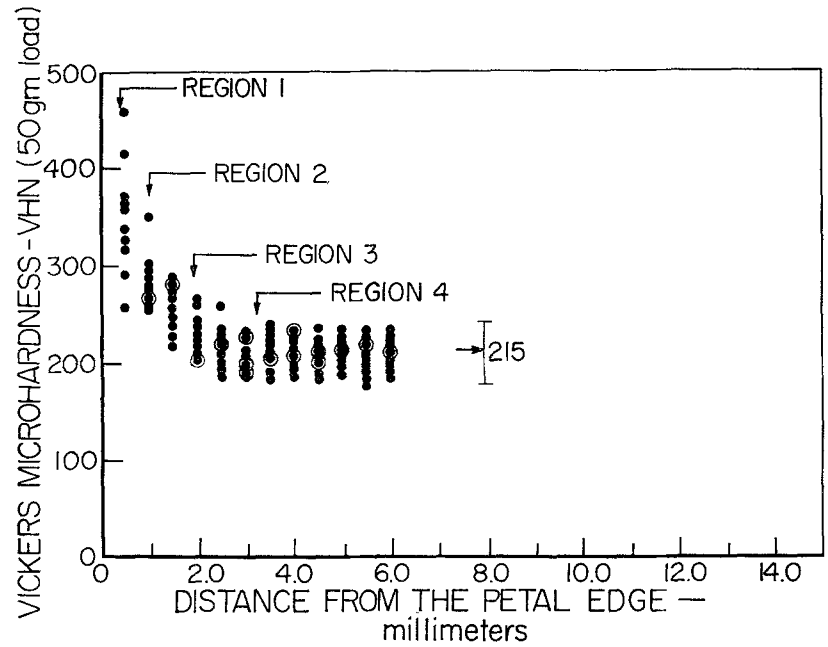

Figure 9 Typical hardness profile data for a petal test strip from the bottom (exit) plate of a 3-plate laminate of Inconel 600. Points plotted represent hardness values corresponding to the exit surface of the test strip. The undeformed sheet hardness is indicated as 215, and characterised roughly by region 4. The designated regions refer to the approximate locations of areas observed by transmission electron microscopy.

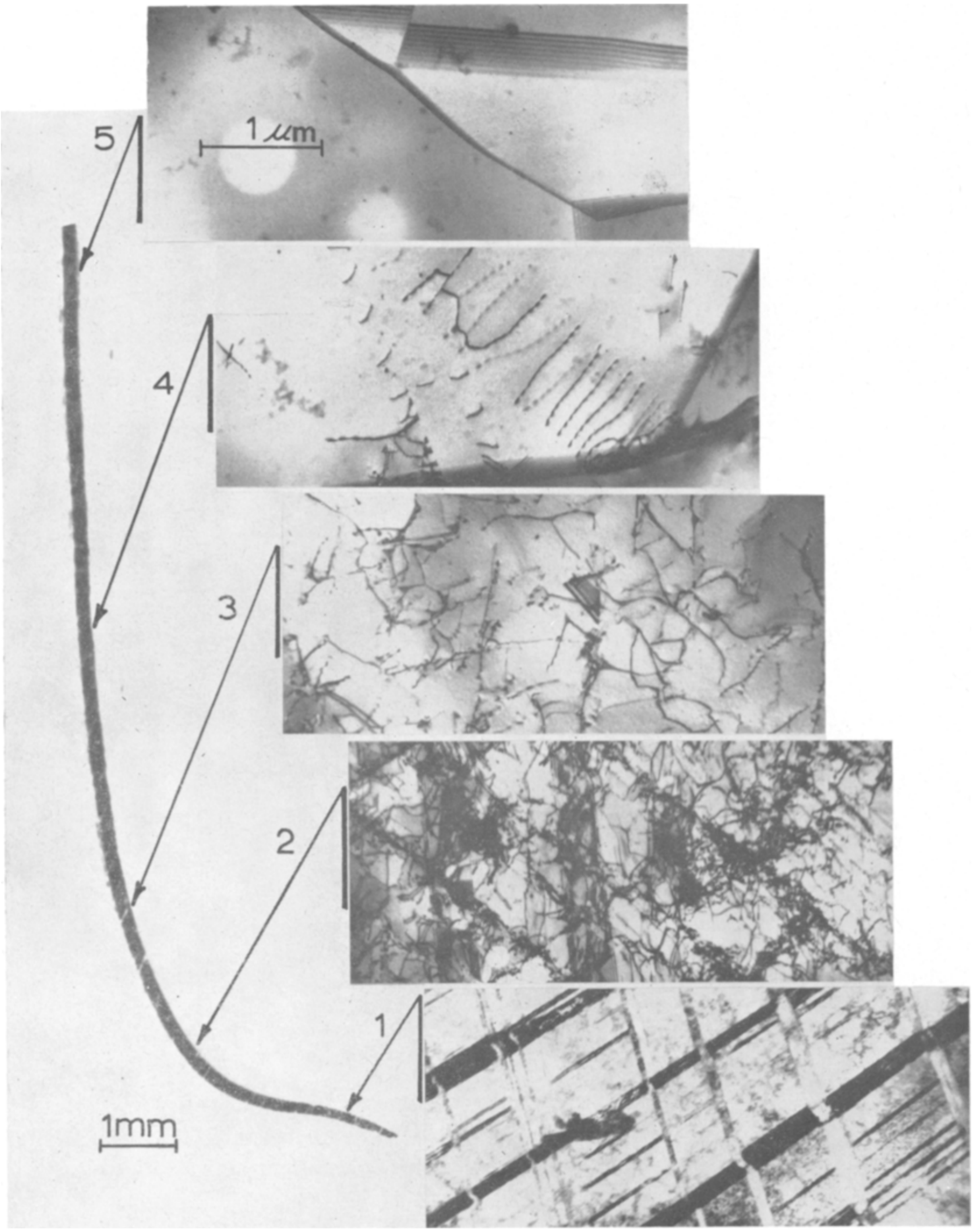

Figure 10 Selected-area transmission electron micrographs of the petal regions of a .22 calibre bullet hole in a thin stainless steel plate. The location designations (1 to 5) correspond to the hardness regions of fig. 8 as indicated for the accompanying petal section view. Observations were made for petal sections from the exit plates of 3-plate laminates. The approximate surface orientations in regions 1 to 3 are (1 1 0).

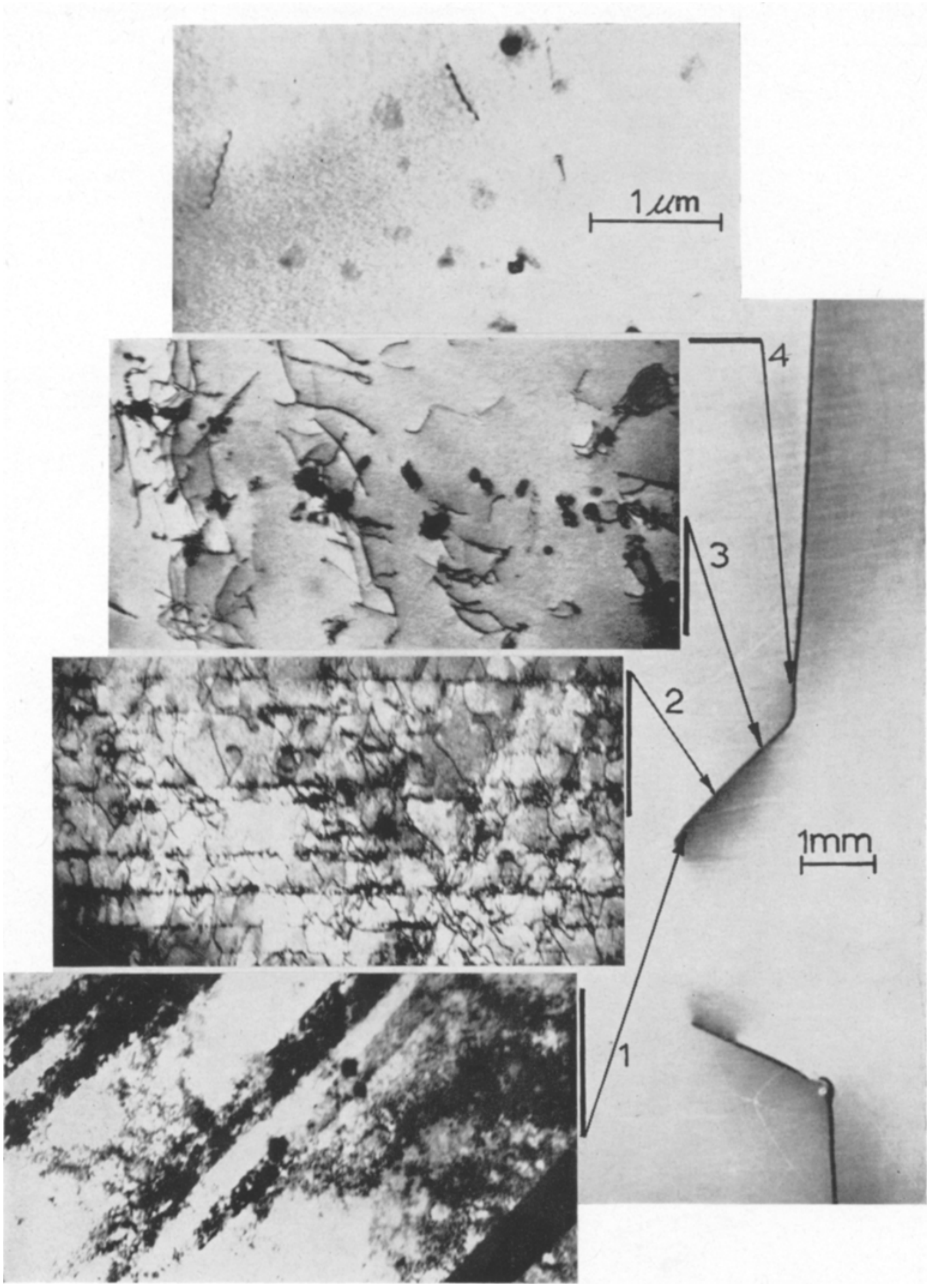

Figure 11 Selected-area transmission electron micrographs of the petal regions of a .22 calibre bullet hole in a thin Inconel plate. The location designations (1 to 4) correspond to the hardness regions of fig. 9 as indicated for the accompanying perforation section view. Observations were made for petal sections from the exit plates of 3-plate laminates. The approximate surface orientations in all regions shown are (1 1 0).

detachment of the cap, and the concomitant friction between the contacting surfaces.

Measurements of the dislocation densities within the hardness regions indicated in figs. 8 and 9, and observed in figs. 10 and 11, are portrayed in the curves of fig. 12. The points plotted represent an average of measurements made over a total area of at least 200 μm^2 distributed over approximately six different image locations using the method of Ham [22];

$$\Lambda = \frac{2N}{Lt}, \tag{17}$$

where N is the total number of intersections of dislocation lines with square grid lines of total length L over an area of foil having a thickness t. In each area examined the operating reflection for dislocation contrast was noted in the corresponding selected-area electron diffraction pattern, and the average dislocation density measured was corrected as discussed by Hirsch and Steeds [23] for that fraction of dislocations out of contrast and invisible in the image.

As stated previously, the residual deformation microstructures in the zone of action for various thicknesses of material penetrated were essentially identical for corresponding microhardness regions with reference to figs. 5 and 6. Fig. 13 is evidence of this feature in stainless steel and shows a typical transmission electron microscope image from a petal area in a single stainless steel sheet (0.18 mm thick) perforated as indicated in fig. 7b, and having an average hardness (VHN) of 250 (100 g load). This corresponds roughly to region 3 of figs. 8 and 10, and the similarity to the region 3 image of fig. 10 should be apparent. Examination of the stacking-fault contrast as shown in fig. 13 using bright- and dark-field techniques indicated their nature to be intrinsic.

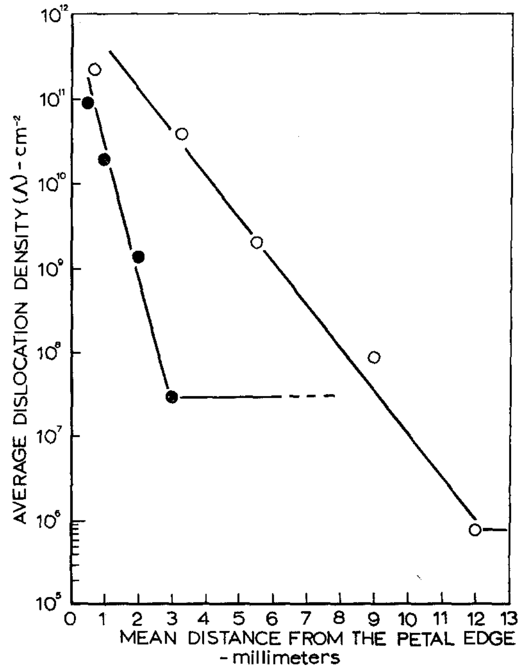

Figure 12 Radial dislocation density distribution in the petals adjacent to .22 calibre bullet holes in thin stainless steel and Inconel sheets, ○, 304 stainless steel; ●, Inconel 600.

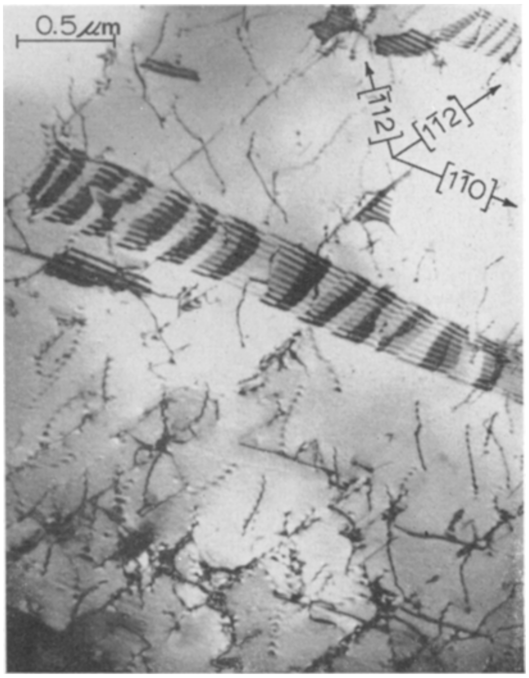

Figure 13 Typical residual microstructures in the petals of a ballistic perforation in a single 0.18 mm thick 304 stainless steel sheet. The image corresponds to a radial distance of approximately 1.5 mm from the petal edge. The coincidence of stacking-faults and planar dislocation arrays with the calculated crystallographic directions attests to the nearly exact (1 1 0) surface orientation.

Examination of the extracted caps by transmission electron microscopy revealed a residual microstructure essentially identical to that for the petal edge (~ 0.5 mm from the petal edge) of corresponding thicknesses perforated in both the stainless steel and Inconel. Consequently, a considerable deformation twin density was observed in the detached caps for both stainless steel and Inconel perforations. Fig. 14 shows a

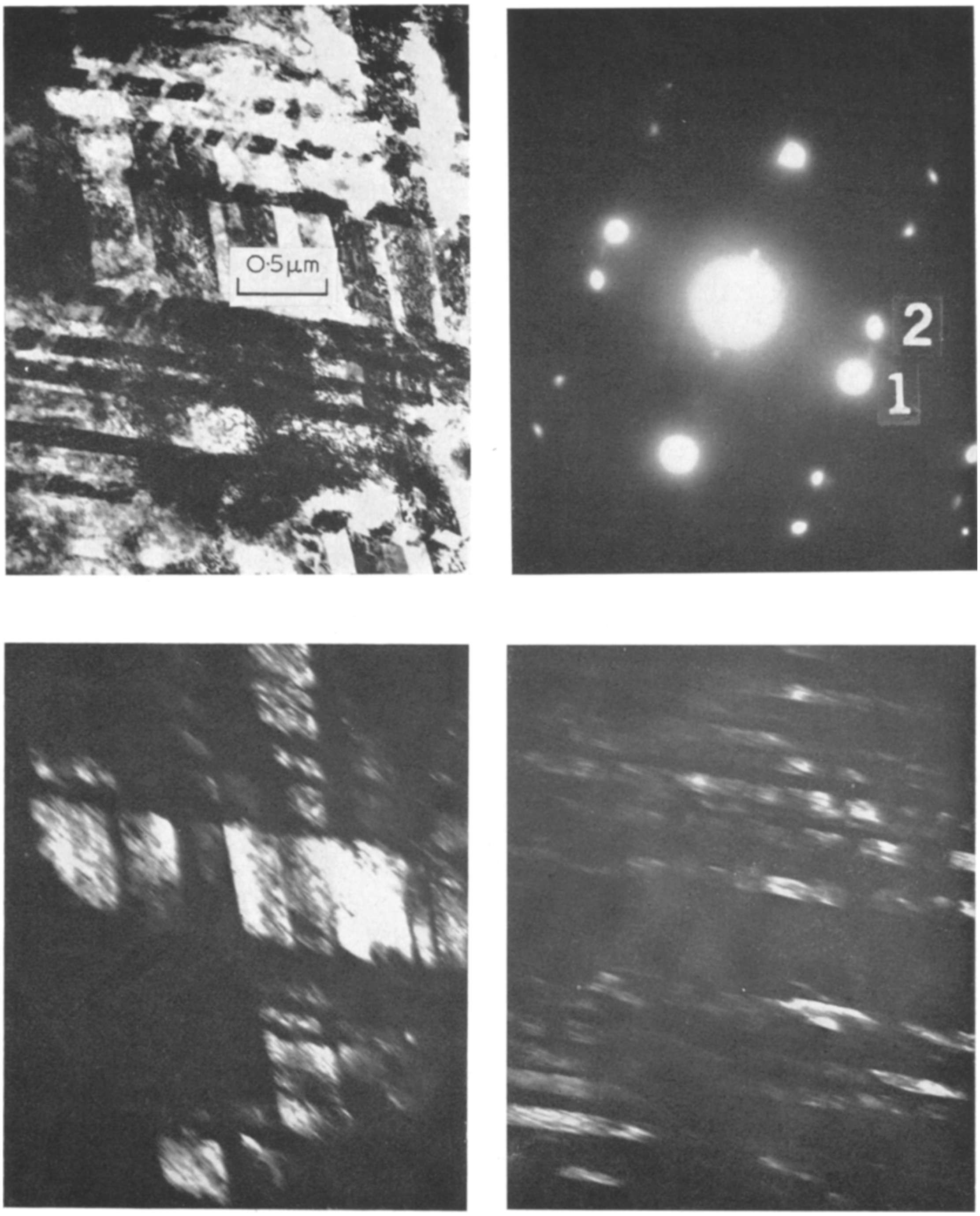

Figure 14 Bright- and dark-field transmission electron micrographs of deformation twin structures in the detached cap from a bullet hole in a 3-plate laminate of 304 stainless steel. Upper left micrograph shows bright-field image. Upper right shows selected-area electron diffraction pattern for slightly tilted (1 0 0) orientation. Lower left micrograph shows corresponding dark-field image with objective aperture over reflection 1 indicated in the electron diffraction pattern. Lower right micrograph shows corresponding dark-field image with objective aperture over reflection 2 indicated in the electron diffraction pattern.

typical area in the cap for a 3-plate laminate of stainless steel corresponding to fig. 10, and having a residual-average microhardness of 410 (100 g load). The average dislocation density in the cap regions from single and laminate perforations of the stainless steel was observed to be about the same as that indicated in fig. 12 at the petal edge. However, the dislocation densities averaged approximately 5 × 10^{11} cm^{-2}, consistent with the residual microhardness responses indicated in fig. 6.

The deformation twin densities (vol %) in the petal edges and caps of the stainless steel and Inconel were computed from

$$A(T) = \bar{W}_T\, 10^2 \sum_j \left(\frac{L_j}{A_j \sin \theta_j}\right), \qquad (18)$$

where $\bar{W}_T$ is the average twin width determined from image detail as described previously [19], L is the total length of twin boundaries inclined at an angle θ with the surface planes over an area A of foil. The average volume densities in the petal edges were found to be 29 and 15% in the perforated stainless steel and Inconel respectively, while the average volume density of twinned material in the caps was found to be approximately 28 and 20% for the stainless steel and Inconel respectively. These calculations were based on an average measured twin width ($\bar{W}_T$) of 200 Å in the petal edges and central cap regions of both materials.

Examination of the bullet holes in the varying thickensses of both materials revealed the physical characteristics to be distinctly different, especially with regard to the formation of petals. As noted previously, the stainless steel perforations were characterised by considerable dishing, with petals less well-defined than those of the Inconel perforations. The petalling characteristics of these materials are compared in the curves plotted in fig. 15. The points plotted in fig. 15 represent the averages for all plates of a laminated sample, or single plate specimens, with the number of petals formed in the same thickness of sample perforated again averaged. The form of these curves attests to the deformation process as summarised in equation 16.

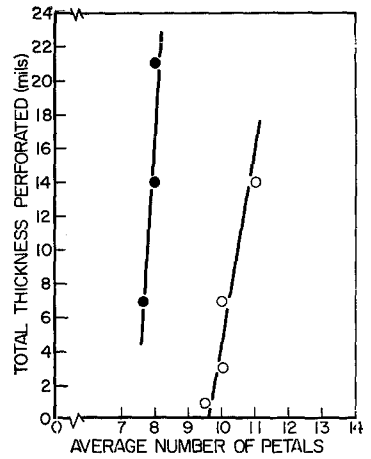

Figure 15 Petal response for .22 calibre bullet hole formation in thin stainless steel and Inconel sections. ●, 304 stainless steel; ○, Inconel 600.

As a means to obtain an approximate measure of the total strain involved in the perforation process the diameter of the residual hole with the petals and perforated edges rolled back into the original plane was averaged for equivalent thickness perforations for each material, and this diameter compared with the diameter of the flattened cap for the corresponding perforations. In effect, the total residual strain becomes

$$\epsilon = \frac{D_c - D_h}{D_h}, \qquad (19)$$

where D_c is the diameter of the flattened-extracted cap, and D_h is the diameter of the hole with the petals rolled back. Fig. 16 shows the curves which resulted for perforations where the caps could be recovered. It must be noted that fig. 16 indicates the corresponding total strain

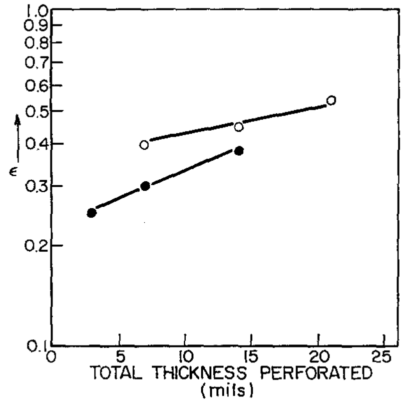

Figure 16 Total residual strain measured for ballistic perforations by .22 calibre bullets in 304 stainless steel and Inconel 600 section thicknesses. ○, stainless steel; ●, Inconel. 1 mil = 0.025 mm.

measurements for the complete perforation process. Thus, we might effectively write

$$\epsilon = \epsilon_{\mathrm{f}} + \epsilon_{\mathrm{P}}, \tag{20}$$

where ϵ_{f} is the total strain to fracture, and ϵ_{P} is the residual straining of the petals following the separation of the cap as perforation is completed. It might also be emphasised that ϵ_{f} represents the stretching of the target (high strain rate tension) plus the residual strain due to shearing of elements in a direction parallel to the direction of motion of the projectile.

5. Discussion

The results of this investigation indicate quite clearly the character and extent of deformation substructures associated with ballistic perforation of thin sheet materials. Of particular interest is perhaps the occurrence of microtwins in the petal edges and the cap region, a feature presumably representative of stage III work-hardening associated with the fracture and separation of the cap in the formation of the bullet hole.

We might consider here in retrospect the analytical features of this problem as outlined previously, namely that ballistic penetration and perforation probably involve shock-wave propagation, elastic-plastic stretching of the target in the zone of action (R_{lim} of fig. 3), and shearing in a direction parallel to the axis of the projectile. The elastic-plastic responses will undoubtedly be governed by high strain-rate effects, but since the mode of deformation, particularly fracture and detachment of the cap from the cratered thin sheet, is so complex, it is difficult to characterise precisely.

Fig. 17 shows for comparison the residual deformation twin structures in (a) the petal edge of a single (0.18 mm) sheet ballistic perforation of stainless steel, (b) a machined chip of stainless steel having an initial depth of cut of 0.3 mm, and (c) a typical sample section of explosive-plane shock-loaded stainless steel. In fig. 17b, with a machining rate of 11.15×10^{-2} cm sec^{-1}, the cutting force was measured as 336 kg for a steel tool with an effective 30° rake angle. Using a dynamic shear stress of 7450 kg cm^{-2}, the calculated shear strain was computed to be 1.82, and this value is considerably greater than the strain measurements recorded in fig. 16. However, the direct measurement of twin volume density based on a twin width ($\bar{W}_{\mathrm{T}}$) of approximately 250 Å resulted in a value of 43% [24]. Similarly, the twin volume density in fig. 17c, representative of stainless steel shock-loaded to 425 kbar with a pulse duration of about 2 μsec, was found to be 44% for a twin width ($\bar{W}_{\mathrm{T}}$) of 150 Å. These latter values of twin volume density are to be compared with that measured in this investigation, and represented in fig. 17a, for the petal edge, i.e. 29 vol %.

Fig. 18 also shows for comparison the

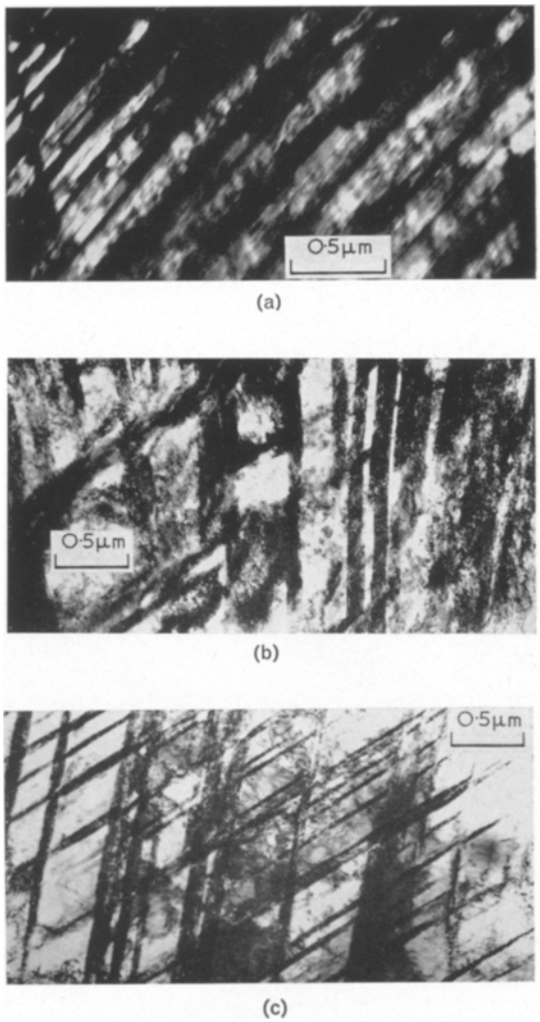

Figure 17 Deformation twins in 304 stainless steel observed for various modes of deformation. (a) Dark-field image of twins in the petal edge of a single sheet ballistic perforation. (b) Bright-field image of twins in machined chip for a depth of cut of 0.3 mm. (c) Bright-field image of twins following explosive shock deformation at 425 kbar. The grain surface orientations in (a) and (b) are approximately (1 1 0); and (1 1 2) in (c).

deformation twin structure in (a) the petal edge of an Inconel perforation (0.09 cm) with that typically observed in explosive-plane shock-loaded Inconel (fig. 18b) at a peak pressure of 370 kbar, and a pulse duration of about 2 μsec. The twin volume density in fig. 18b was measured to be 19% considering an average twin width, $\bar{W}_T$, of 150 Å. This twin volume density is to be compared with 15 vol % measured for the petal edges in perforated Inconel as shown in fig. 18a, and previously in fig. 11.

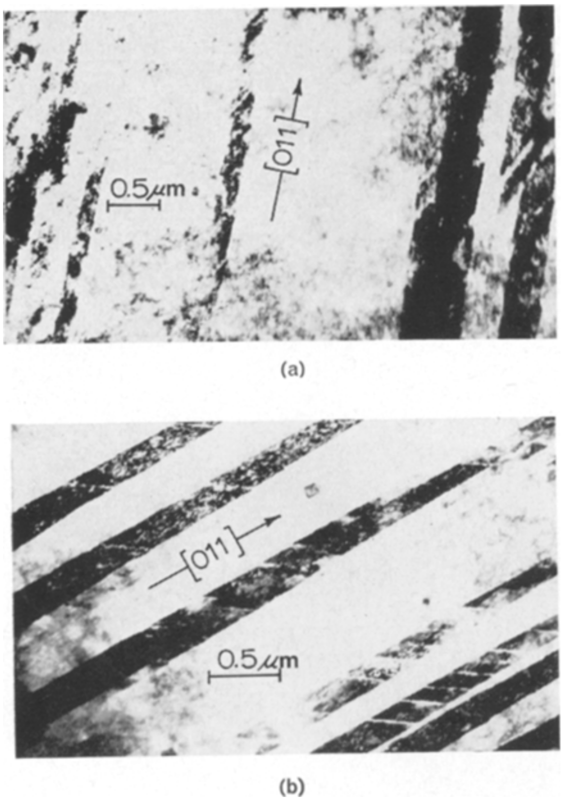

Figure 18 Bright-field images of deformation twins in Inconel 600 observed for ballistic perforation in the petal edge (a), and following explosive shock deformation at 370 kbar (b); both in approximately (1 0 0) orientation.

As a means of estimating the stress induced in the cap by the ballistic impact, a set of typical parameters characterising the cap formation in the stainless steel sheet were considered as follows: $m = 2.59$ gm, $v_s = 40\,540$ cm sec^{-1}, $t_0 = 0.0531$ cm (0.021 in. thick sheet), and $\rho = 7.86$ gm cm^{-3}. The radius of the hemispherical bullet head was measured as $a = 2$ mm. To obtain a reasonable value of r_f and σ_Y, sub-size tensile specimens 2.5 cm in length and 0.318 cm wide were cut from the stainless steel test sheet. Stress(load)-strain(elongation) measurements were then made on several of these specimens in a Tinius-Olsen load-compensated tensile tester using a gauge length of 1.588 cm (inked symmetrically on the specimens), and a cross-head speed of 0.25 cm min^{-2}, giving rise to a strain rate of roughly 2.7×10^{-3} sec^{-1}. As indicated in fig. 19, tensile fracture occurred for a corresponding strain of approximately 0.40. Settings $\mathrm{d}S/\mathrm{d}r_0 = 1.4$ and using equations 3, 4 and 9, we obtain $r_f = 1.82$ mm. With an average value of $\sigma_Y \simeq 4569$ kg cm^{-2}, we find that $\Delta W_P = 1.03 \times 10^7$ ergs, and the corresponding pressure in the cap along the direction of motion to be $\bar{\sigma} = 6.6$ kbar.

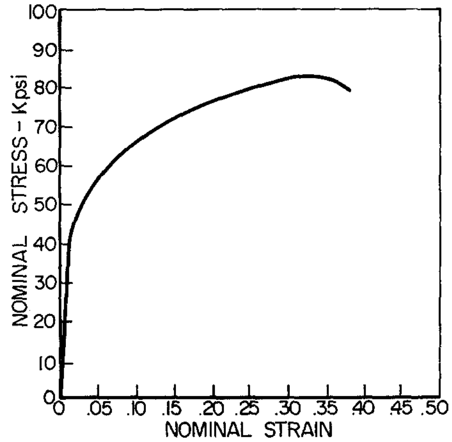

Figure 19 Nominal stress-strain curve for 304 stainless steel sheet tested in tension at a strain rate of 2.7×10^{-3} sec^{-1}.

Since contact pressures during ballistic penetration do not exceed about 10 kbar in the stainless steel sheet (and presumably also in the Inconel), and considering further that deformation twins do not occur in either stainless steel or Inconel shock-loaded to pressures less than about 150 kbar [16, 19], it appears unlikely that shock effects contribute significantly to the perforation processes considered in this investigation. In effect, it must be assumed that the formation of deformation twins in the petal edges and caps of both stainless steel and Inconel occurs primarily as a result of shear parallel to the direction of projectile motion and/or strain-rate effects. This assumption must be taken with some reservations since we have no knowledge of triaxial strain effects in shock-loaded materials. However, the absence of defects beyond the zone of action, R_{lim}, generally attests to the absence of shock effects.

Very little is known of the rate-dependence of the stress/strain characteristics of materials in the range 10^{-3} to 10^{3} $\sec^{-1}$, and no attempts have been made to evaluate these phenomena in the range of $\sim 10^{6}$ $\sec^{-1}$ which dominates high-velocity penetration. Early work by Manjoine [26] has indicated that mild steel, for instance, tested at room temperature in a strain-rate range of 10^{-7} to 10^{3} $\sec^{-1}$, shows a consistent increase in the total strain to fracture ($\sim$ 0.27 to 0.42). However, more recent investigations of effects of strain-rate on the stress/strain curves of some fcc metals (Cu, Ni, Al) shock-loaded or cold-rolled prior to testing indicate that in copper for example, the total strain to fracture decreases with increasing strain rate (in the range 10^{-5} to 10^{-2} $\sec^{-1}$) for previously shock-loaded samples, and increases with increasing strain-rate for cold-rolled samples [27]. Banks [28] has also recently investigated high-rate (explosive) loading of cylinders and found the strain-to-fracture to increase with expansion velocity for commercial grades of aluminium and carbon steels.

If we now compare the perforation strain data of fig. 16 for stainless steel with the tensile strain to fracture shown in fig. 19, it is observed that the total residual perforation strain for a single sheet of the material exceeds the tensile fracture strain by approximately 0.05. Thus, if we rigorously apply the analytical considerations outlined previously, perforation can be adequately explained in terms of macroscopic stress/strain theory by considering this difference in residual strain to reflect either a strain-rate dependence, or the strain in the petals following fracture, ϵ_P, as indicated phenomenologically in equation 20. However, as we consider fig. 17b, we would be tempted to seriously consider shear effects to predominate if the rate-dependence of the stress/strain properties is negligible during high-velocity perforation. Since there has been no experimental evidence of the occurrence of deformation twins in stainless steel failed in tension at conventional high strain rates ($< 10^{3}$ cm^{-1}), such an assumption may be valid.

It is to be noted in figs. 8 to 12 that the zone of action (R_{lim} of fig. 2) is considerably less in Inconel, for equivalent thicknesses perforated, than that of stainless steel. Furthermore, the zone of action in each material is characterised by the presence of recognisable defects (dislocations). Since this zone effectively defines the extent of local deformation, it is obvious from figs. 10 and 11 that to characterise thin plate penetration or perforation from the considerations of elasticity theory is unrepresentative of the material response. A realistic approach must involve the plastic, work-hardening characteristics of the material. Thus, resistance to perforation or penetration will be dependent to a large extent upon the generation and propagation of crystal imperfections, and the physical properties which regulate these processes, e.g. stacking-fault free energy. It is presumed, in this respect, that the presence of precipitates in the Inconel matrix, to act as dislocation sources and barriers to the motion of dislocations, can account for some of the observed differences (fig. 11).

It might also be mentioned that preliminary calculations of the temperature rise in the cap at the instant of detachment from the plate indicated a maximum temperature of approximately 300° C for both the stainless steel and Inconel sheets (0.18 and 0.03 mm respectively). Since this temperature is considerably less than the recrystallisation temperature for both materials, it appears unlikely that the residual microstructures reflect any thermal annealing effects.

6. Summary and Conclusions

We have attempted to demonstrate, in this investigation, the powerful new approach to the analysis of thin plate perforation afforded by the direct observation of the residual deformation substructures by transmission electron microscopy. In addition, it was desired to demonstrate that classical analytical treatments of such a problem can, for the most part, be supplemented in substance by visual information concerning residual defect density and character which should ultimately prove of great value in devising new armouring materials.

As cautioned in the introduction of this paper, it is impossible to characterise completely the perforation process by the present approach, or perhaps any approach, in a single experiment. The aim of this presentation has been simply to demonstrate the feasibility of a direct approach, and to illustrate the utility of this approach. It is particularly important to convey in this presentation the fact that the techniques outlined herein are not limited to the specific problem of bullet hole analysis. Rather, it is hoped the possible applications to such phenomena as penetration and perforation of thin-skinned aircraft, meteoric perforation of spacecraft and civil and military armouring have also been clearly indicated.

Considering the results presented in this investigation, the following conclusions are noted:

(i) The zone of action (R_{lim} of fig. 2) completely describes the associated range of deformation accompanying perforation in a thin material, and deformation as evidenced by the presence of residual defects does not extend beyond the deviation of petal or dishing curvature from the plane of the undeformed plate.

(ii) The characteristics of bullet holes in thin sheets of stainless steel and Inconel are noticeably different, on comparison, with respect to the extent of deformation (the radius of the zone of action, R_{lim}) and the degree of petalling accompanying ballistic perforation. This is due in part to the reduced Inconel ductility because of the fine precipitate present.

(iii) Deformation in the petals following the formation of a bullet hole in thin stainless steel and Inconel sheets is characterised by the formation of deformation microtwins in the petal edges and over the volume of the cap, with a transition to stacking-faults and dense planar arrays in stainless steel with a stacking-fault energy of 22 ergs cm^{-2}, dense planar dislocation arrays in the Inconel having a stacking-fault energy of 28 ergs cm^{-2}, dislocation densities decreasing radially from the petal edges.

(iv) Dislocations generated at the incoherent precipitate-matrix interface, which results as the Inconel sheet is penetrated, as well as impedance to dislocations provided by these precipitates, presumably account in part for the different perforation properties exhibited on comparing stainless steel and Inconel. The difference in the nature of the residual defect structures is also due in part to the difference in stacking-fault free energy of these materials as noted in (iii).

(v) The mode of deformation associated with the fracturing of the cap, and petalling during the formation of a bullet hole in ductile thin sheet materials is a combination of high-velocity shear and strain-rate effects. In particular, the fracture process is presumably influenced by these phenomena.

(vi) Direct observations by transmission electron microscopy of residual deformation substructures in thin sheet materials subject to high strain-rate punching, high-velocity and hypervelocity impact and perforation can provide a new and powerful approach to materials evaluation and fabrication, specific to these areas of technology.

Acknowledgements

The authors express their sincere thanks to R. J. Horylev and W. N. Lin for their assistance in various aspects of the experimental work, and to Frank Withopf, Cinema Division, for his help in preparing fig. 7. Partial support of this work by NASA Multidisciplinary Research Grant NGL-05-018-044 (1480) and Joint Services Electronics Grant AFOSR-69-1622 is also gratefully acknowledged. Special thanks are also due to Cliff Warner, Cepiad Associates, Boalsburg, Penna., for the professional renderings of our original illustrations, and Dr F. I. Grace, NWL, for commenting on the original manuscript.

References

1. J. S. RINEHART and J. PEARSON, "The Behavioi of Metals Under Impulsive Loads" (ASM, Cleveland, 1954).
2. W. GOLDSMITH, *Appl. Mech. Rev.* **16** (1963) 855.
3. W. GOLDSMITH and P. T. LYMAN JR, *J. Appl. Mech. Trans. ASME* Series E, **27** (1960) 717.
4. G. I. TAYLOR, *Quart. J. Mech. and Appl. Math.* **1** (1948) 103.
5. A. J. WANG and H. G. HOPKINS, *J. Mech. and Phys. of Solids* **3** (1954) 22.
6. M. ZAID and B. PAUL, *J. Franklin Inst.* **264** (1957) 117.
7. *Idem, ibid.* **268** (1959) 24.
8. J. NISHIWAKI, *J. Phys. Soc. Japan* **6** (1951) 374.
9. W. GOLDSMITH, T. W. LIU, and S. CHULAY, *Exp. Mech.* **5** (1965) 385.
10. H. A. BETHE, Frankford Arsenal Rpt. No. UN-41-5-23 (1941).
11. W. T. THOMPSON, *J. Appl. Phys.* **26** (1955) 80.
12. C. J. MAIDEN, *Phil. Mag.* **3** (1958) 1413.
13. J. W. CRAGGS, *Proc. Roy. Soc.* **A63** (1962) 369.
14. A. B. J. CLARK, W. F. HASSEL, and J. M. KRAFFT, *Naval Res. Lab. Memo* Rpt. 150, May (1959).
15. Elements of Armament Engineering, US Army Material Command, AMCP 706-107, September (1963).
16. M. C. INMAN, L. E. MURR, and M. F. ROSE, *Adv. Electron Metal* (*ASTM*) **STP 396** (1966) 39.
17. L. E. MURR and M. F. ROSE, *Phil. Mag.* **18** (1968) 281.
18. F. I. GRACE, M. C. INMAN, and L. E. MURR, *Brit. J. Appl. Phys.* **1** (1968) 1437.
19. L. E. MURR and J. V. FOLTZ, *J. Appl. Phys.* **40** (1969) 3796.

20. L. E. MURR and A. B. DRAPER, *Proc. Electron Microscopy Soc. Amer.* 26th Anniversary Volume (1968) 442.
21. L. E. MURR, *Appl. Materials Res.* **3** (1964) 153.
22. R. K. HAM, *Phil. Mag.* **6** (1961) 1183.
23. P. B. HIRSCH and J. W. STEEDS, "Relation Between the Structure and Mechanical Properties of Metals" NPL Symposium No. 15 (1964) p. 39; see also Table 17.1, p. 423 of P. B. HIRSCH, *et al*, "Electron Microscopy of Thin Crystals" (Butterworths, London, 1965).
24. A. B. DRAPER, L. E. MURR, and B. F. TURKOVICH, to be published.
25. C. HWANG, *J. Appl. Mchs. Trans. ASME* Series E, **26** (1959) 594.
26. M. J. MANJOINE, *J. Appl. Mechs.* **11** (1944) 211.
27. A. S. APPLETON and J. S. WADDINGTON, *Phil. Mag.* **12** (1965) 273.
28. E. E. BANKS, *J. Inst. Met.* **96** (1968) 375.

Received 8 August and accepted 2 October 1969.